Title: Variation of Jupiter's Aurora Observed by Hisaki/EXCEED: 3. Volcanic Control of Jupiter's Aurora

Paper: GRL

Authors: Chihiro Tao [1, 2], Tomoki Kimura [3], Fuminori Tsuchiya [2], Go Muirakami [4], Kazuo Yoshioka [5], Atsushi Yamazaki [4], Sarah V. Badman [6], Hiroaki Misawa [2], Hajime Kita [2], Yasumasa Kasaba [2], Ichiro Yoshikawa [5], Masaki Fujimoto [4]

Affiliations:

[1] NICT, Koganei, Japan
[2] Tohoku University, Sendai, Japan
[3] Riken, Saitama, Japan
[4] ISAS/JAXA, Sagamihara, Japan
[5] University of Tokyo, Chiba, Japan
[6] Lancaster University, Lancaster, England

Corresponding Author: Chihiro Tao (chihiro.tao@nict.go.jp)
Running title (<=45 characters): Io's volcanic effect on Jovian aurora (37)
Abstract&text 3437 + Figure caption 465 = 3902
Figure 3+ Table 1
UNIT= 8+4=12

Key points (<=140 characters):

1. Responses of Jupiter's northern aurora spectra to Io volcanic activity were detected using Hisaki/EXCEED long-term monitoring (125)

2. Decrease of colour ratio, i.e., auroral electron energy, suggests reduced electron acceleration for the more highly populated magnetosphere (139)

3. Long-term observation provided the typical value and variances of auroral emission power and electron parameters (112)

Question 1. *Major Topic or Scientific Question

The major topic is the response of the Jovian magnetosphere/aurora to plasma produced by Io volcanic activity, motivated by the scientific question "What is the role of Io plasma in Jupiter's magnetosphere?"

The plasma source is an important factor in a Jupiter-type rotation-driven magnetosphere.

Question 2. *New Scientific Knowledge

Io volcanic activity modifies Jovian magnetospheric activity via thermal plasma population and the magnetosphere–ionosphere coupled current system. Rapid publication is required because this study has implications regarding Juno and Juno-supporting observations that are currently ongoing.

Question 3. *Broad Implications

This work represents an advance in the area of planet-magnetosphere-moon interaction, which has relevance for communities involved in studies of the internal (planetary) and external (magnetospheric) fields related to current and future missions to Jupiter (e.g., Juno, JUICE). The provided typical and variation values related aurora is useful information for modelling studies.

Abstract

[1] Temporal variation of Jupiter's northern aurora during enhanced Io volcanic activity was detected using the EXCEED spectrometer onboard the Hisaki Earth-orbiting planetary space telescope. It was found that in association with reported Io volcanic events in early 2015, auroral power and estimated field-aligned currents were enhanced during day of year 40–120. Furthermore, the far ultraviolet colour ratio decreased during the event, indicating a decrease of auroral electron mean energy and total acceleration by <30%. During the episode of enhanced Io volcanic activity, Jupiter's magnetosphere contains more source current via increased supra-thermal plasma density by upto 42%; therefore, it would have required correspondingly less electron acceleration to maintain the enhanced field-aligned current and corotation enforcement current. Sporadic large enhancements in auroral emission detected more frequently during the active period could have been contributed by non-adiabatic magnetospheric energization. (137 words)

1. Introduction

59 [2] The Jovian magnetosphere is characterized by a plasma supply of up to ~1 ton s^{-1} from its
60 volcanically active moon, Io. Despite the initial radial transport of the plasma, its rotational motion
61 around Jupiter is maintained by the transfer of angular momentum from the planetary atmosphere
62 [e.g., Hill, 1979]. Jupiter's main aurora is considered to be produced by the angular momentum
63 transfer carried by the field-aligned current [e.g., Hill, 2001; Cowley and Bunce, 2001].

64 [3] The level of volcanic activity of Io can change dramatically; the subsequent enhancement in the
65 emission of the Io plasma torus (IPT) can persist for a few days to a period of several months. In
66 association with the volcanic activation in May 2007 detected via brightening of the sodium nebula
67 observation by Yoneda et al [2009], an auroral image after the enhancement showed an equatorward
68 shift of the main aurora and an increase in the occurrence of very bright enhancement >600 GW at
69 lower latitudes [Bonfond et al., 2011]. On the other hand, the activity of aurora-related hectometric
70 radio emission was reduced [Yoneda et al., 2013]. As momentum transfer is supposed to occur
71 efficiently over a more limited radial distance of the equatorial magnetosphere for the increased
72 plasma case, theoretical models predict that the main aurora would be located at lower latitudes for
73 the case of increased Io plasma mass loading [Nichols and Cowley, 2005; Tao et al., 2010; Nichols,
74 2011]. Nichols [2011] suggested that the field-aligned current, i.e., intensity of the main auroral
75 emission, would increase or decrease when variation in plasma production occurs with or without the
76 modification of the background plasma density, respectively. In order to associate these different
77 features of the aurora (i.e., auroral intensity and particle acceleration) with the resultant auroral
78 electron energy, continuous auroral spectral observation is required.

79 [4] This monitoring can be achieved by JAXA's Hisaki Earth-orbiting space telescope. The
80 EXCEED (Extreme Ultraviolet Spectroscope for Exospheric Dynamics) spectrometer onboard

Hisaki monitors emissions from both the IPT and Jupiter's northern aurora simultaneously [Yoshioka et al., 2013; Yoshikawa et al., 2014; Yamazaki et al., 2014]. Ground-based monitoring of the sodium line from Jupiter magnetosphere showed enhancement and radial extension on the eastern side starting from 10 January 2015 (day of year (DOY) 10) [Yoneda et al., 2015]. Infrared imaging of Io's surface detected a sudden brightness enhancement at Kurdalagon Patera on 26 January [de Kleer and de Pater, 2016]. The intensity of emission rom the sodium neutral cloud subsequently increased by almost a factor of four by the middle of February before decreasing in April. This emission enhancement is actually weak compared to typical events [Yoneda et al., 2015]. This variation in neutral sodium emission was followed by enhancements of IPT S^+ (increase from DOY 20 and decrease during DOY ~60–90), S^{2+} (increase from DOY ~30 and decrease during DOY 70–110), and S^{3+} lines (increase from DOY ~40 and decrease from DOY 90) detected by EXCEED [Tsuchiya et al., 2017MOP, Yoshikawa et al., 2017]. EXCEED cannot resolve auroral structure due to its moderate spatial resolution (~1 R_J around Jupiter's opposition), but it can monitor auroral spectra continuously for ~40 min during each 106-min orbit. Applying the spectral analysis proposed by Tao et al. [2016a, 2016b] (hereafter Paper I and Paper II, respectively), the auroral and magnetospheric responses to the described volcanic activity are investigated in this study.

2. Observations and Data Procedure

[5] The Hisaki auroral observations and analysis are described in detail for the reader by Kimura et al. [2015], Paper I, and Paper II, therefore we only describe them briefly herein. The northern auroral region is covered by the dawn–dusk directed dumbbell-shaped slit with an effective spatial resolution of 17 arcsec and a pointing accuracy of ±2 arcsec. EXCEED detects auroral emissions over the 80–148 nm wavelength range, covering part of the H_2 Lyman and Werner band emissions with full width

103 at half maximum (FWHM) resolution of 0.3 nm. The auroral signals within the 20 arcsec aperture of
104 the slit width are integrated for each specific wavelength. The waveband 138.5–144.8 nm is used to
105 estimate the total emission and input power. The far ultraviolet colour ratio (CR) is defined as the
106 ratio of the intensity of the waveband absorbed least by atmospheric hydrocarbons (138.5–144.8 nm)
107 to that absorbed most (123–130 nm), which for EXCEED is defined as CR_{EXCEED}. As the CR reflects
108 the depth of the auroral electron precipitation into the hydrocarbon layer, the auroral electron energy
109 can be estimated assuming a particular atmosphere model. The total number flux derived from the
110 electron energy and energy flux is converted into the field-aligned current density, using an averaged
111 auroral area based on an empirical magnetic field model called VIP4 [Connerney et al., 1998]. With
112 reference to the auroral electron acceleration theory, the source current density can then be estimated
113 (Paper II). We analysed observations when the Jupiter northern aurora was facing Earth, i.e., when
114 the central meridional longitude (CML) was 45–345° system III longitude. As the auroral oval
115 around the northern pole is shifted from Jupiter's rotational pole, the auroral aperture and thus the
116 auroral power detectable from Earth varies with Jupiter's rotation. This aperture effect on the total
117 power is scaled by multiplying by the factor, (maximum visible auroral length integrated over all
118 CML)/(visible auroral length at instantaneous CML), assuming a typical auroral location (Paper II),
119 which is called "revised power" hereafter.

120 [6] The solar wind conditions just upstream of Jupiter's magnetosphere are estimated using a
121 one-dimensional magnetohydrodynamic model that propagates the solar wind variation observed at
122 Earth toward Jupiter [Tao et al., 2005]. Here, we used OMNI 1-hour data as the input for this
123 propagation model.

124 **3. Results**

125 [7] Figure 1 shows an overview of the variation of the auroral parameters (Figures 1a–1c) and the
126 IPT power (Figure 1d) for two periods: season 2014 (December 2013 to April 2014) and season 2015
127 (November 2014 to May 2015). Auroral intensity enhancements can be observed in
128 minimum-hydrocarbon absorption wavebands within the Hisaki/EXCEED wavelength range (Figure
129 1a) and the total emitted power (Figure 1b). These are associated with the enhancement of the source
130 current density $j_{//0}(2.5/k_B T_0$ [keV]) before the field-aligned acceleration of the magnetospheric
131 electrons occurs (Figure 1c). Several enhancements over a few days during the observation periods
132 are related to enhancements due to the solar wind dynamic pressure (Figure 1e), whereas the aurora
133 shows a characteristic variation associated with the long-term IPT enhancement (Figure 1d). All
134 estimated parameters are provided in the supplementary material (Figure S1).

135 [8] Compared with season 2014 and the early part of season 2015 (until DOY40), the aurora shows
136 larger enhancements more frequently after DOY40 in 2015. With reference to the more continuous
137 observations in season 2015, auroral enhancements beyond 50 GW in the 136.5–144.8 nm waveband
138 can be seen on DOY –33 to –32, –7, 12–14, 41, 48–49, 66, 70, 72, 74, 87, 96, 103, 116, and 127 in
139 2015 (Figure 1a), i.e., 3 events in the first 80 days (DOY –40 to 40) and 11 events in the second 80
140 days (DOY 40–120).

141 [9] Among them, very large enhancements of the power in the 136.5–144.8 nm waveband reach 115,
142 105, and 173 GW on DOY 66, 74, and 87 in 2015, respectively. As the emission intensity of
143 maximum-hydrocarbon absorption waveband (126.3–130.0 nm) also increases (Figure S1b), the CRs
144 and electron energies for these events are not large; their medians and standard deviations (1σ) of the
145 electron energy are 165 ± 38, 165 ± 23, and 159 ± 31 keV, respectively, slightly smaller than the
146 value of 178 ± 39 keV derived from the entire data set within a statistically insignificant level

147 (0.33σ–0.49σ, where σ=39 keV). On the other hand, their electron fluxes reach 282, 268, and 431
148 MA, which are 5.2, 5.0, and 7.9 times larger than the mean value over the entire period, respectively.

149 [10] Figure 2a shows the CR_{EXCEED} as a function of CML comparing before (DOY 0–30, blue) and
150 after (50–80, red) the volcanic activity enhancement. CR_{EXCEED} at CML175–225° decreases
151 significantly during the active period by up to 30%. We divided the data into two groups: auroral
152 power enhancement events (EV, red points in Figures 2b–2d) whose revised auroral power at 136.5–
153 144.8 nm reaches >45 GW and other backgrounds (BG, black points). As discussed above, the
154 occurrences of these events vary. 10-day running averages of both EV and BG show a decrease in
155 CR_{EXCEED} after DOY ~40 in 2015 (Figure 2c), and a slight increase in electron flux (Figure 2d) with
156 almost constant power (Figure 2b) is seen for BG.

157 [11] Table 1 lists the median values of the key parameters over five selected periods: (i) season 2014,
158 (ii) DOY -40 to 40, (iii) DOY 40 to 120, (iv) DOY 120 to 140 of season 2015, and (v) the entire
159 dataset. The error values represent the standard deviation. The standard deviation of the emission
160 power, electron flux, and source current density increase during the period of Io enhanced activity,
161 e.g., the standard deviation of the revised total emission power is 1175 GW in (iii) and 493–512 GW
162 in the other periods.

163 [12] Figure 3a shows the relationship between the mean electron energy and energy flux taken from
164 the active (period (iii), orange points) and other quiet periods (periods (ii) and (iv), black points) in
165 season 2015. For the active period, the mean energy decreases as seen in Figure 2c and energy flux
166 mainly increases with a broadening of its distribution. The difference between the two distributions is
167 evident in the contour maps of each period shown in Figures 3b and 3c. We derived best-fit Knight
168 relation curves with a density of source 2.5 keV electrons that minimizes the root mean squared error

(RMSE) of the data. We used 90% data points which have energy flux and mean energy values closest to the average of each value. Moreover, the density becomes 0.0019 and 0.0027 cm^{-3} during the quiet and active periods, respectively. The goodness of fit is confirmed by a good distributional correlation between the concentrations of data shown in red (27% occurrence), with the white curves representing the best-fit Knight relation curves. The derived minimum RMSEs for these two periods are relatively small such that their difference is statistically significant. The best-fit curves for the constant source density (0.0019 cm^{-3}) correspond to a source electron temperature of 1.3 keV for the active period, suggesting another possibility for this change.

[13] The median value of the revised power is also largest in period (iii), followed in descending order by periods (i), (ii), and (iv). Auroral power is modulated by solar wind dynamic pressure [Kita et al., 2016]. A linear relation between auroral power and solar wind was derived using the information at (ii) 0.037 and (iv) 0.021 nPa. For the pressure of 0.049 nPa of (iii), the total power derived from this linear relation is 1279 GW, which is slightly smaller than the observed power of 1355 GW but the difference is not significant compared to the error averaged over the whole period, 281 GW.

[14] The total energy emitted over 800 points (1 point =10 min.) before (10.4<DOY2015<52), during (45.8<DOY2015<82.5), and after (97.2<DOY2015<140) the volcanic active period are 6.0×10^{8} J, 7.6×10^{8} J, and 6.4×10^{8} J, respectively. Differences among the volcanic activity phases are much larger than 2.9×10^{5} J, derived using the mean error. Additionally, the total energy input into the polar region during the entire event reaches 2×10^{19} J, which is comparable with the total energy content of the magnetospheric ions ~1.4×10^{19} J [Bagenal and Delamere, 2011].

4. Discussion

191 [15] In the auroral feature, we found the following characteristic variations: (i) enhancements of the
192 auroral power and its variation were caused by sporadic short-term (<1 rot to a few days)
193 enhancements (Figure 1), and (ii) a relatively small colour ratio, i.e., auroral electron energy (Figures
194 2 and 3a–3c), observed during DOY 40–120 of 2015. It is known that volcanic eruptions (outbursts)
195 last days, and the torus enhancement lasts from a few to tens of days. For this volcanic event in early
196 2015, the increase in infrared emission at Kurdalagon Patera was observed on DOY26, sodium
197 emission began on DOY10 until its peak on ~DOY50 [e.g., Yoneda et al., 2015], and OI emission
198 began on DOY20 and peaked during DOY40–60 [Koga et al., 2018]. Moreover, plasma transfer from
199 the IPT (~6 R_J) to the middle magnetosphere of the main auroral source region (~20 R_J) is suggested
200 to take tens of days [Bagenal and Delamere, 2011]. Therefore the variations observed during
201 DOY40–120 reflect an enhanced plasma transfer at the middle magnetosphere. There are other
202 periods with smaller CR and sporadic enhancements at the beginning of season 2015, e.g., DOY-40
203 to -10. This might have been affected by another volcanic event in late 2014, as reported by de Kleer
204 and de Pater [2016]; this was prior to the Hisaki and sodium monitors, and therefore beyond our
205 dataset. First, we qualitatively compare these parameters with the quiet period, followed by
206 comparison with previous findings obtained using different methods.

207 [16] Hisaki's long-term monitoring provides the following statistical auroral parameters: the total
208 electron flux precipitation into the polar region of 54.2±30 MA and appearance-revised total
209 emission power of 1276±810 GW. The total electron flux is comparable with the plasma
210 corotation-enforcement current of 60–100 MA derived as a curl of the magnetic field measurement
211 [Khurana, 2001]. The revised total power is also comparable with other analyses, e.g., 1.2 TW
212 [Badman et al., 2016].

213 [17] For the auroral enhancement event of season 2014, the enhancement of the source current
214 density is comparable with the magnetospheric adiabatic variation due to solar wind compression
215 (see Section 5.4 of Paper II for detail). The other possible process, i.e., the positional change toward
216 an open–closed boundary, is less probable here, referring to observation of auroral deposition toward
217 low latitudes during the interval of increased Io plasma mass loading reported by Bonfond et al.
218 [2011] and theoretical suggestions [e.g., Nichols and Cowley, 2005].

219 [18] We apply the same analysis to the 66 events in 2014–2015 seasons whose revised power at
220 136.5–144.8 nm exceeds 45 GW. We refer to the maximum value of solar wind dynamic pressure
221 over four days (from two days before to two days after the events), and the minimum value of the
222 pressure over two days before the maximum pressure. These time spans are set by taking into
223 account the solar wind model uncertainty of shock arrival and possible time lag of magnetospheric
224 response. Magnetopause location is derived from the solar wind pressure using an empirical model
225 [Huddleston et al., 1998]. We estimated the density increase due to the magnetospheric compression
226 assuming isotropic shrinking under the conservation of mass, and corresponding plasma temperature
227 variation for the adiabatic change to obtain variation of the source current $j_{//0}$. Then the field-aligned
228 current density for the observed electron energy is derived referring to the Knight theory. We
229 compare the estimated increase ratio of the field-aligned current, R_{model}, with that directly estimated
230 from the auroral spectral observation, R_{obs}. Figure 4a shows the relationship between R_{model} and R_{obs}.
231 Since this model is based on the solar wind pressure variation, we exclude the events which are
232 independent of the solar wind pressure enhancement (maximum pressure <0.1 nPa, 13 events) shown
233 by small marks. If the variation follows this model, the relationship should be $R_{model}=R_{obs}$.
234 Eighty-one percent of all events are $R_{obs}/R_{model}<2$. Some events which deviated from the relationship,

i.e., larger $R_{model}/R_{obs} \geq 2$, are more frequently seen for the volcanic activity cases (seven red points) compared to the quiet case (two blue points). In addition, the R_{obs}/R_{model} values increase with the increasing R_{obs}. This deviation from $R_{obs}=R_{model}$ indicates the contribution of the other processes beyond the above model and assumptions, e.g., non-adiabatic plasma acceleration such as magnetospheric reconnection and local heating, especially for the volcanic active period and large enhancement events.

[19] As seen in Figure 3, during the active volcanic phase, the typical relationship between the auroral mean energy and the flux shifts in a number of ways, e.g.: (i) to the more magnetospheric populated case, i.e., from 0.0019 to 0.0027 cm^{-3}, or (ii) to a lower temperature of the source plasma, i.e., from 2.5 keV to 1.3 keV, for the constant density case, or a combination of both. According to Nichols [2011], as an increase in the auroral electron flux is achieved in the case corresponding increase in background density, we will discuss the plasma increase, above case (i). Note that this population is the thermal electron (~a few keV) which can reach the planetary atmosphere compared with the more abundant cold component (~tens eV) in the magnetosphere. This indicates that the energetic supra thermal electrons are also increased by the volcanic activity, while the neutrals and ionized plasma enhanced at IPT would be mainly the cold component. In addition, the estimated auroral electron energy decreases for the active period, indicating a smaller acceleration. This behaviour likely arises because the greater population of the source plasma would be enough to maintain the corotation enforcement current with less electron number energy enhancement. A spectral diagnosis of the IPT emission observed by Hisaki suggests the enhancement of the cold (~several eV) and hot (~100s eV) electron density during the period of Io enhanced activity [Kagitani et al., 2017MOP; Yoshikawa et al., 2017], and also indicates that the hot electron

257 population increases with distance from Jupiter [Yoshioka et al., 2017]. Although there is a
258 difference in radial distances between the location of IPT (~6 R_J) and the magnetospheric source
259 region of the main aurora (~20 R_J), the auroral analysis additionally suggests the enhancements of
260 the supra thermal plasma in the middle magnetospheric. According to a modelling study by Nichols
261 [2011], the enhancement of the total current seen in this observation also supports the increase of the
262 magnetosphere plasma population with increased plasma mass loading at Io. The plasma angular
263 velocity deviates from the corotation at smaller radius with more rapid variation during the increased
264 plasma mass-loading period. This provides a larger magnetospheric current as well as a field-aligned
265 current, which has been observed as an increase in auroral emission power [Nichols, 2011].

266 [20] Using spatially resolved auroral spectra, Gérard et al. [2016] (and partly Gustin et al. [2004] and
267 Paper I) showed that the relation between auroral electron energy/CR and electron energy flux varies
268 according to which specific auroral feature is considered. The relationship derived from the
269 polar-integrated Hisaki dataset is the spatially-averaged characteristic, as discussed in Paper I. In
270 addition, the estimated electron energies in this study are mean values and we cannot specify the
271 auroral electron spectral change in detail, i.e., whether a decrease of electron energy over the whole
272 energy range, or a relative decrease (increase) of high (low) energy electrons, or a combination of
273 these types of changes. These are open questions beyond the scope our dataset and present analysis.
274 We need to develop additional methods to ascertain in case other acceleration processes are
275 dominant.

276 **5. Summary**

277 [21] Long-term monitoring of Jupiter's aurora by Hisaki/EXCEED has detected enhancements of the
278 auroral power with a strong sporadic response (by a factor of 2) and a decrease in the colour ratio,

279 i.e., the auroral electron energy (by upto 30%), associated with reported Io volcanic events observed
280 in early 2015. The enhanced plasma mass-loading of Io increases the source current via an increased
281 supra-thermal (a few keV) plasma density by upto 42%, which contributes to a large field-aligned
282 current to maintain the corotation with less field-aligned acceleration. Sporadic large auroral
283 enhancements during the interval are not readily explained by an adiabatic solar wind response
284 model, which suggests a contribution by non-adiabatic magnetospheric energization.

285 **Acknowledgements**

286 [21] We acknowledge the working teams of Hisaki/EXCEED, WIND, ACE, and OMNI. The data
287 from the Hisaki spacecraft can be found in the Data Archives and Transmission System (DARTS) of
288 JAXA. The OMNI data used for the solar wind model were taken from the NASA Coordinated Data
289 Analysis Web (CAWeb). This work was supported by MEXT/JSPS KAKENHI Grant JP15K17769.
290 We acknowledge the contribution of the International Space Sciences Institute (ISSI) in Bern,
291 Switzerland, for hosting and funding the ISSI international teams on “The influence of Io on
292 Jupiter’s magnetosphere” (ID388) and “How does the solar wind influence the giant planet
293 magnetospheres?” (ID357) and the constructive discussions had by these team members. We thank
294 NASA/PSP members for useful discussions.

295

296 **References**

297 Badman, S. V., et al. (2016), Weakening of Jupiter's main auroral emission during January 2014,
298 *Geophys. Res. Lett., 43*, 988–997, doi:10.1002/2015GL067366.

299 Bagenal, F., and P. A. Delamere (2011), Flow of mass and energy in the magnetospheres of Jupiter
300 and Saturn, *J. Geophys. Res., 116*, A05209, doi:10.1029/2010JA016294.
301 Bonfond, B., M. F. Vogt, J.-C. Gérard, D. Grodent, A. Radioti, and V. Coumans (2011),
302 Quasi-periodic polar flares at Jupiter: A signature of pulsed dayside reconnections?, *Geophys. Res.*
303 *Lett., 38*, L02104, doi:10.1029/2010GL045981.
304 Connerney, J. E. P., M. H. Acuña, N. F. Ness, and T. Satoh (1998), New models of Jupiter's
305 magnetic field constrained by the Io flux tube footprint, *J. Geophys. Res., 103*(A6), 11,929–
306 11,939, doi:10.1029/97JA03726.
307 Cowley, S. W. H., and E. J. Bunce (2001), Origin of the main auroral oval in Jupiter's coupled
308 magnetosphere-ionosphere system, *Planet. Space Sci., 49*, 1067–1088.
309 de Kleer, K., and I. de Pater (2016), Time variability of Io's volcanic activity from near-IR adaptive
310 optics observations on 100 nights in 2013–2015, *Icarus, 280*, 378-404.
311 Gérard, J.-C., B.Bonfond, D.Grodent, and A.Radioti (2016), The color ratio-intensity relation in the
312 Jovian aurora: Hubble observations of auroral components, *Planet. Space Sci., 131*, 13–23.
313 Gustin, J., J.-C. Gérard, D. Grodent, S. W. H. Cowley, J. T. Clarke, and A. Grard (2004),
314 Energy-flux relationship in the FUV Jovian aurora deduced from HST-STIS spectral observations,
315 *J. Geophys. Res., 109*, A10205, doi:10.1029/2003JA010365.
316 Hill, T. W. (1979), Inertial limit on corotation, *J. Geophys. Res., 84*(A11), 6554–6558.
317 Hill, T. W. (2001), The Jovian auroral oval, *J. Geophys. Res., 106*(A5), 8101–8107.
318 Huddleston, D. E., C. T. Russell, M. G. Kivelson, K. K. Khurana, and L. Bennett (1998), The
319 location of the Jovian bow shock and magnetopause: Galileo initial results, *Adv. Space Res., 21*,
320 11, 1463–1467.

321 Kagitani, M., M. Yoneda, R. Koga, F. Tsuchiya, K. Yoshioka, G. Murakami, T. Kimura, I.
322 Yoshikawa (2017), Variation of ion and electron temperature on Io plasma torus during an
323 outburst measured with Hisaki/EXCEED and gourd-based telescope, Magnetospheres of the
324 Outer Planets (MOP) conference abstract.
325 Khurana, K. K. (2001), Influence of solar wind on Jupiter's magnetosphere deduced from currents in
326 the equatorial plane, *J. Geophys. Res., 106*(A11), 25999–26016, doi:10.1029/2000JA000352.
327 Kimura, T., et al. (2015), Transient internally driven aurora at Jupiter discovered by Hisaki and the
328 Hubble Space Telescope, *Geophys. Res. Lett., 42*, doi:10.1002/2015GL063272.
329 Kita, H., et al. (2016), Characteristics of solar wind control on Jovian UV auroral activity deciphered
330 by long-term Hisaki EXCEED observations: Evidence of preconditioning of the magnetosphere?,
331 *Geophys. Res. Lett., 43*, 6790–6798, doi:10.1002/2016GL069481.
332 Koga, R., F. Tsuchiya, M. Kagitani, T. Sakanoi, M. Yoneda, K. Yoshioka, T. Kimura, G. Murakami,
333 A. Yamazaki, I. Yoshikawa, and H. Todd Smith (2018), The time variation of atomic oxygen
334 emission around Io during a volcanic event observed with Hisaki/EXCEED, *Icarus, 299*, 300–
335 307.
336 Nichols, J. D. (2011), Magnetosphere-ionosphere coupling in Jupiter's middle magnetosphere:
337 Computations including a self-consistent current sheet magnetic field model, *J. Geophys. Res.*,
338 *116*, A10232, doi:10.1029/2011JA016922.
339 Nichols, J. D., and S. W. H. Cowley (2005), Magnetosphere-ionosphere coupling currents in Jupiter's
340 middle magnetosphere: Effect of magnetosphere-ionosphere decoupling by field-aligned auroral
341 voltages, *Ann. Geophys., 23*, 799–808.

342 Tao, C., R. Kataoka, H. Fukunishi, Y. Takahashi, and T. Yokoyama (2005), Magnetic field
343 variations in the Jovian magnetotail induced by solar wind dynamic pressure enhancements, *J.*
344 *Geophys. Res., 110*, A11208, doi:10.1029/2004JA010959.
345 Tao, C., H. Fujiwara, and Y. Kasaba (2010), Jovian magnetosphere-ionosphere current system
346 characterized by diurnal variation of ionospheric conductance, *Planet. Space Sci., 58*, 351–364,
347 doi:10.1016/j.pss.2009.10.005.
348 Tao, C., et al. (2016a), Variation of Jupiter's aurora observed by Hisaki/EXCEED: 1. Observed
349 characteristics of the auroral electron energies compared with observations performed using
350 HST/STIS, *J. Geophys. Res. Space Physics, 121*, 4041–4054, doi:10.1002/2015JA021271.
351 Tao, C., T. Kimura, S. V. Badman, N. André, F. Tsuchiya, G. Murakami, K. Yoshioka, I. Yoshikawa,
352 A. Yamazaki, and M. Fujimoto (2016b), Variation of Jupiter's aurora observed by
353 Hisaki/EXCEED: 2. Estimations of auroral parameters and magnetospheric dynamics, *J. Geophys.*
354 *Res. Space Physics, 121*, 4055–4071, doi:10.1002/2015JA021272.
355 Tsuchiya, F. et al. (2017), Enhancement of Jovian magnetospheric plasma circulation due to mass
356 supply change from the satellite Io, Magnetospheres of the Outer Planets (MOP) abstract.
357 Yamazaki, A. et al. (2014), Field-of-view guiding camera on the HISAKI (SPRINT-A) satellite,
358 *Space Sci. Rev., 184*, 1–4, 259–274, DOI: 10.1007/s11214-014-0106-y.
359 Yoneda, M., M. Kagitani and S. Okano (2009), Short-term variation of Jupiter's extended sodium
360 nebula, *Icarus, 204*, 589–596.
361 Yoneda, M., F. Tsuchiya, H. Misawa, Bonfond B., Tao C., M. Kagitani and S. Okano (2013), Io's
362 volcanism controls Jupiter's radio emissions, *Geophys. Res. Lett., 40*, 671–675,
363 doi:10.1002/grl.50095.

364 Yoneda, M., M. Kagitani, F. Tsuchiya, T. Sakanoi, and S. Okano (2015), Brightening event seen in
365 observations of Jupiter's extended sodium nebula, *Icaurs, 261*, 31–33
366 Yoshikawa, I. et al. (2014), Extreme ultraviolet radiation measurement for planetary
367 atmospheres/magnetospheres from the earth-orbiting spacecraft (Extreme Ultraviolet
368 Spectroscope for Exospheric Dynamics: EXCEED), *Space Sci. Rev.*, *184*, 1–4, 237–258,
369 DOI:10.1007/s11214-014-0077-z.
370 Yoshikawa, I. et al. (2017), Volcanic activity on Io and its influence on the dynamics of the Jovian
371 magnetosphere observed by EXCEED/Hisaki in 2015, *Earth, Planets and Space--Frontier Letter*,
372 *69*, 110, doi:10.1186/s40623-017-0700-9.
373 Yoshioka, K. et al. (2013), The extreme ultraviolet spectroscope for planetary science, EXCEED,
374 *Planet. Space Sci., 85*, 250–260.
375 Yoshioka, K., et al. (2017), Radial variation of sulfur and oxygen ions in the Io plasma torus as
376 deduced from remote observations by Hisaki, *J. Geophys. Res. Space Physics, 122*, 2999–3012,
377 doi:10.1002/2016JA023691.
378
379

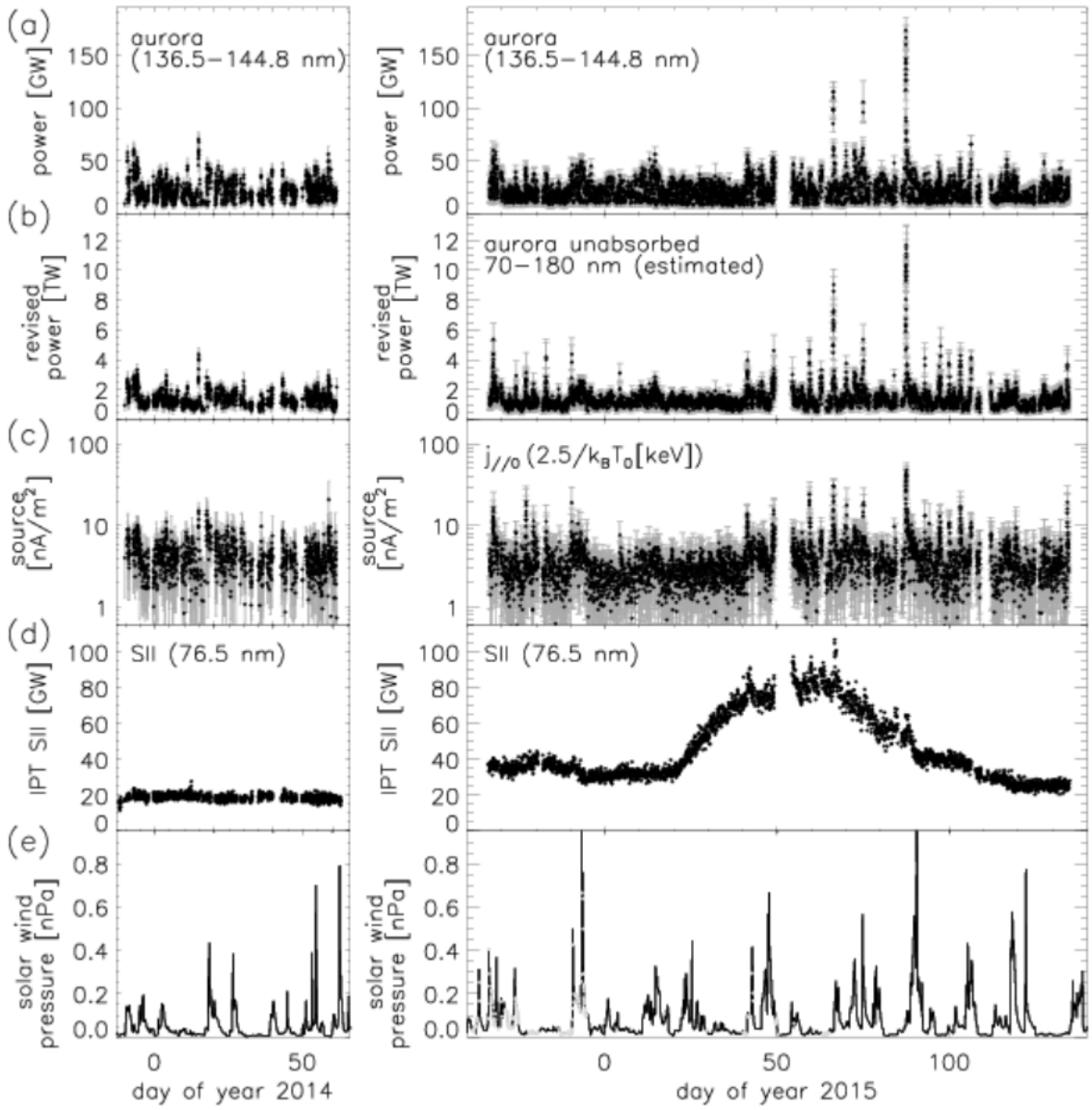

Figure 1. Time variations of the auroral powers emitted at wavelength (a) 138.5–144.8 nm, (b) appearance normalized total unabsorbed H_2 power over wavelength 70–180 nm, (c) maximum field-aligned current that can be carried by precipitating magnetospheric electrons without field-aligned acceleration, shown for the electron temperature k_BT_0 = 2.5 keV case, (d) IPT SII emission (see Yoshikawa et al. [2017] for detail), and (e) solar wind dynamic pressure for season 2014 (left) and season 2015 (right). Grey vertical lines in Figures 1a–1c show errors estimated based

on the photon statistics. Solar wind input data in season 2015 are not complete, which would affect the output grey points in Figure 1e.

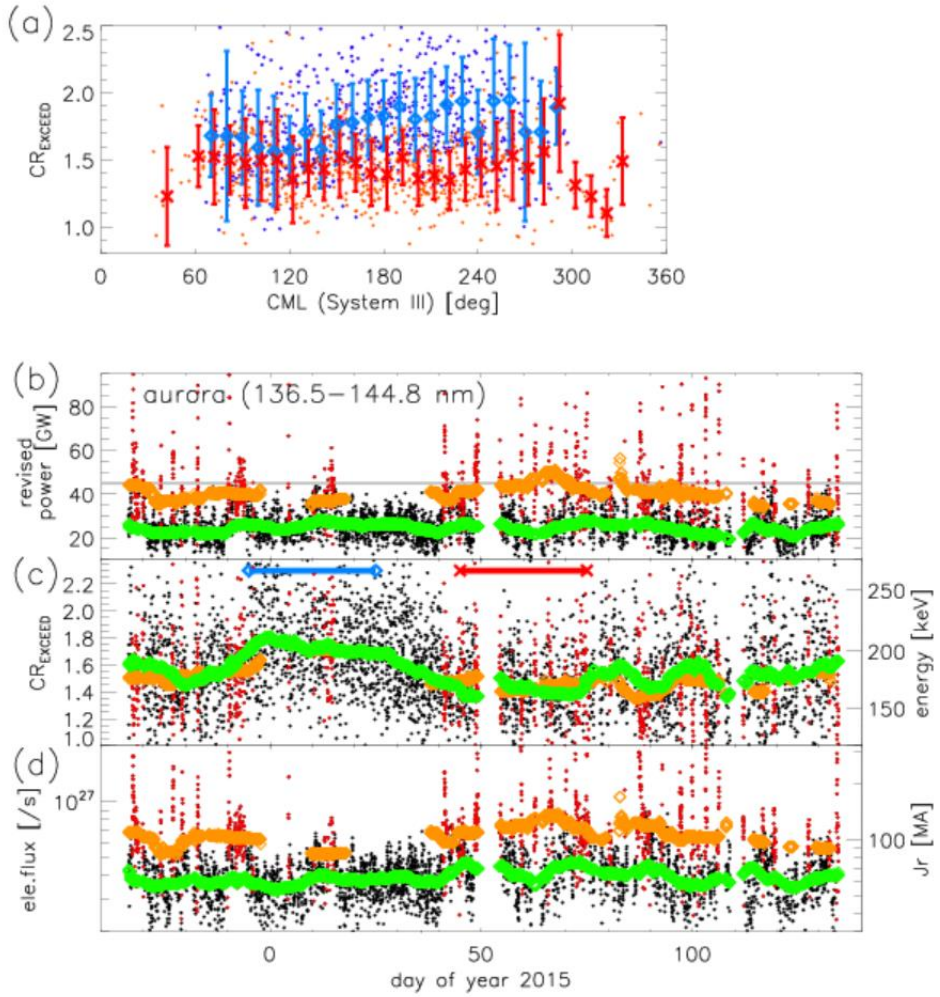

Figure 2. (a) CR_{EXCEED} as a function of CML in system III, and time variations of (b) the power emitted at the wavelength 138.5–144.8 nm, (c) CR_{EXCEED}, and (d) auroral electron flux for season 2015. Blue (red) points in Figure 2a are observed on DOY -5–25 (45–75) in 2015, and diamonds (crosses) are mean values over 10-degree binned CML with error bars showing variances. In Figures 2b–2d, the enhancement event (EV) and backgrounds (BG) are shown by red and black points, respectively, and 10-day running average of EV and BG are shown by orange and green marks, respectively. 45 GW threshold is shown by grey line in Figure 2b. Corresponding auroral electron energy and total current are shown on the right-hand y-axes of Figures 2b and 2c, respectively.

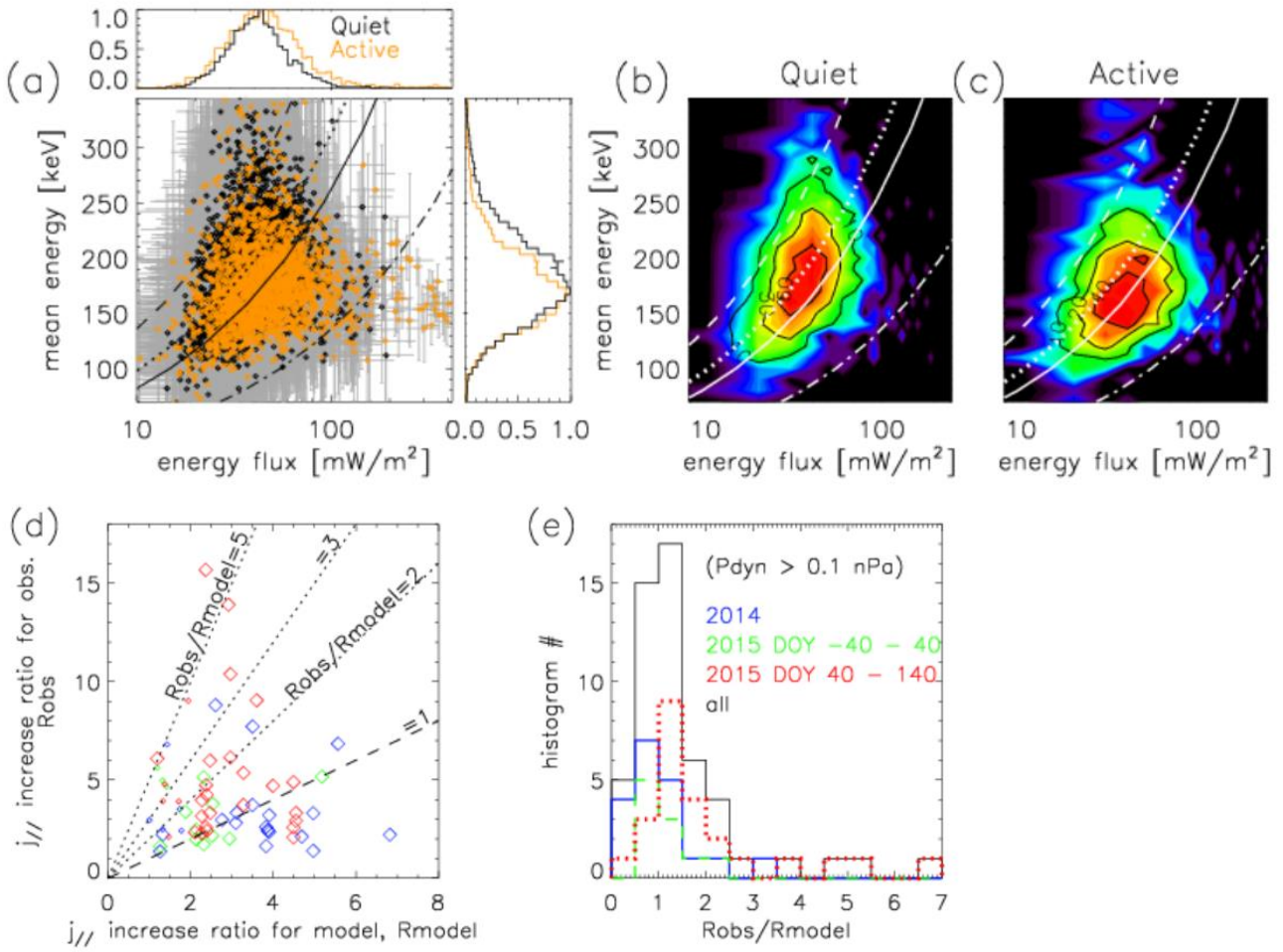

Figure 3. Relationship between the mean energy and energy flux of the precipitating auroral electrons estimated from 10-min integrated observations shown as (a) a scatter plot using data during the quiet (black dots) and active (orange dots) volcanic periods in season 2015, and occurrence map for the (b) quiet and (c) active volcanic periods separately. Grey lines in Figure 3a are error bars, and mean energy and energy flux distributions are plotted as histograms normalized by maximum occurrence values in the right and upper panels, respectively, for each period separately. The Knight relation is shown for different source populations: N_0=0.0027 cm^{-3} (solid lines), N_0=0.0019 cm^{-3} (dotted lines), N_0=0.001 cm^{-3} (dashed lines), and N_0=0.01 cm^{-3} (dotted-dashed lines) [e.g., Gustin et al., 2004]. (d) Increase ratio of the estimated field-aligned current (see text in detail) R_{model},

414 compared with the value derived from the observation, R_{obs}, and (e) histogram of R_{obs}/R_{model} whose
415 solar wind pressure >0.1 nPa. Colour indicates different periods: 2014 seasons (blue), before the Io
416 volcanic active in 2015 (green), and during the active time (red), and sum of them (black in Figure
417 3e). Large diamonds in Figure 3d show the cases whose dynamic pressure reach >0.1 nPa, dashed
418 line shows R_{obs}/R_{model}=1, and dotted lines show R_{obs}/R_{model}=2, 3, and 5.

419

420

421
422
423
424 Table 1. Medians and standard deviations of key parameters during each period.

	(i)2013/12/19-2014/3/3 season 2014	(ii)2014/11/27-2015/2/9 DOY -40 to 40	(iii)2015/2/9-2015/5/18 DOY 40 to 120	(iv)2015/2/23-2015/5/14 DOY 120 to 140	(v)all
Power 138.5-144.8 nm [GW]	21.2±9.69	19.7±8.36	21.8±15.1	18.9±6.94	20.7±11.4
Power 126.3-130.0 nm [GW]	16.4±7.47	13.6±5.71	16.2±11.2	13.5±4.48	15.1±8.45
CR_{EXCEED}	1.42±0.37	1.62±0.36	1.46±0.31	1.54±0.33	1.51±0.35
Electron energy [keV]	167.±37.	191.±41.	171.±35.	181.±38.	178.±39.
Total power [GW]	984.±449.	915.±389.	1009.±701.	871.±324.	962.±529.
Electron Flux [MA]	58.5±26.4	48.9±20.3	58.0±40.1	48.2±15.9	54.2±30.0
Electron Flux [μA m^{-2}]	0.267±0.106	0.216±0.109	0.266±0.254	0.210±0.110	0.243±0.175
$j_{//0}(2.5/k_BT_0$[keV]) [nA m^{-2}]	4.01±2.08	2.88±2.02	3.94±4.22	2.96±2.05	3.42±3.03
Solar wind pressure [nPa]	0.025±0.070	0.037±0.073	0.049±0.117	0.021±0.090	0.032±0.082
System III longitude [deg.]	173. ±61.	176. ±60.	173. ±63.	172. ±54.	174. ±60.
Revised total power [GW]	1311.±493.	1214.±509.	1363.±1175.	1124.±512.	1276.±810.

425

426

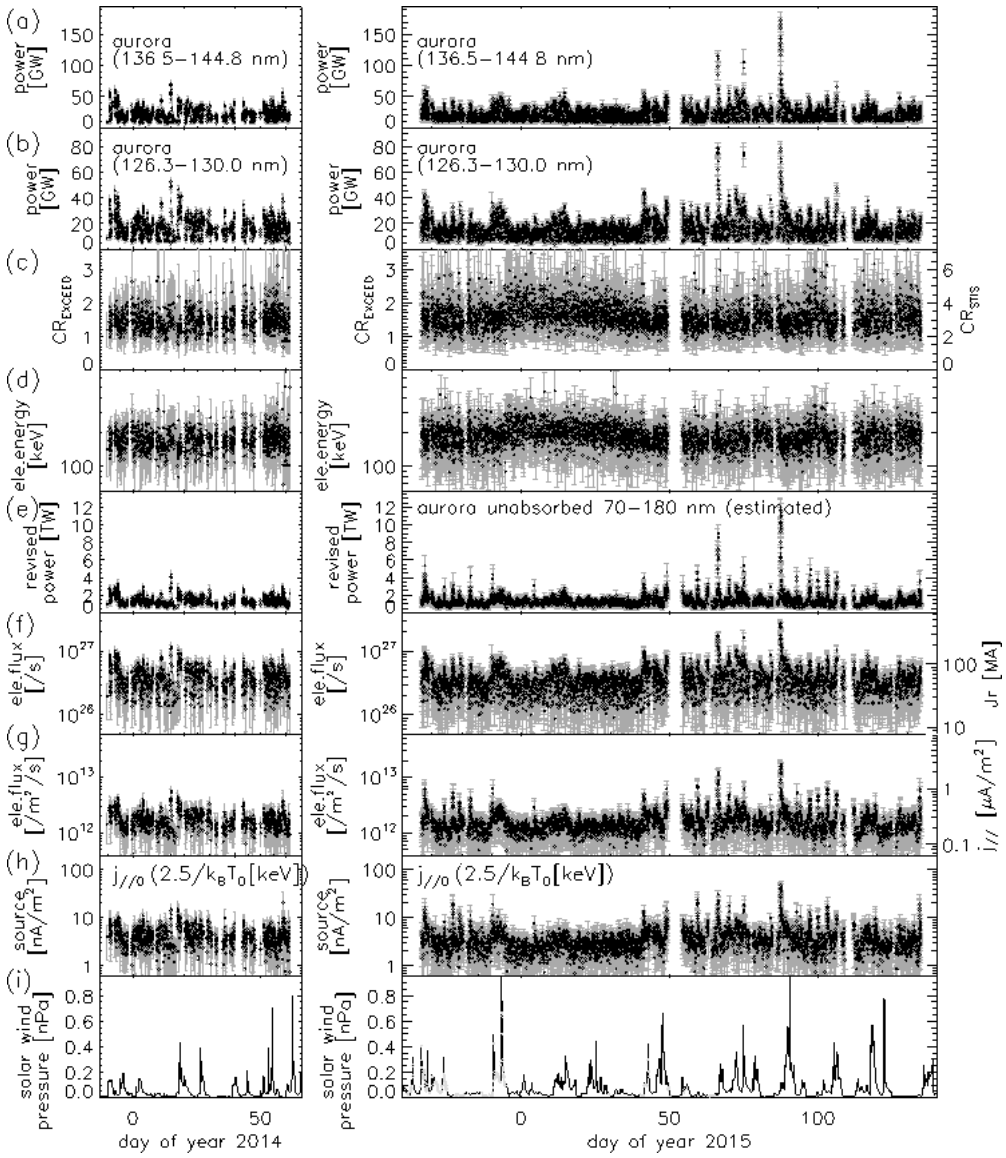

Figure S1. Time variations of the auroral parameters in the same format of Figure 4 of Paper II for seasons 2014 and 2015. From top to bottom, auroral powers emitted at wavelength (a) 138.5–144.8 nm and (b) 126.3–130 nm, (c) CR_{EXCEED}, (d) auroral electron energy, (e) appearance normalized total unabsorbed H_2 power over wavelength 70–180 nm, (f) auroral electron flux and (g) flux density, (h) maximum field-aligned current that can be carried by precipitating magnetospheric electrons without field-aligned acceleration, shown for the electron temperature k_BT_0 = 2.5 keV case, and (i) solar wind dynamic pressure for season 2014 (left) and season 2015 (right). Corresponding typical colour ratio

435 $CR_{STIS} \equiv I_{155–162\ nm}/I_{123–130\ nm}$, total current, and current density are shown on the right-hand y-axes of

436 Figures S1c, S1f, and S1g, respectively. Other formats are the same with the Figure 1.

437

Figure 1.

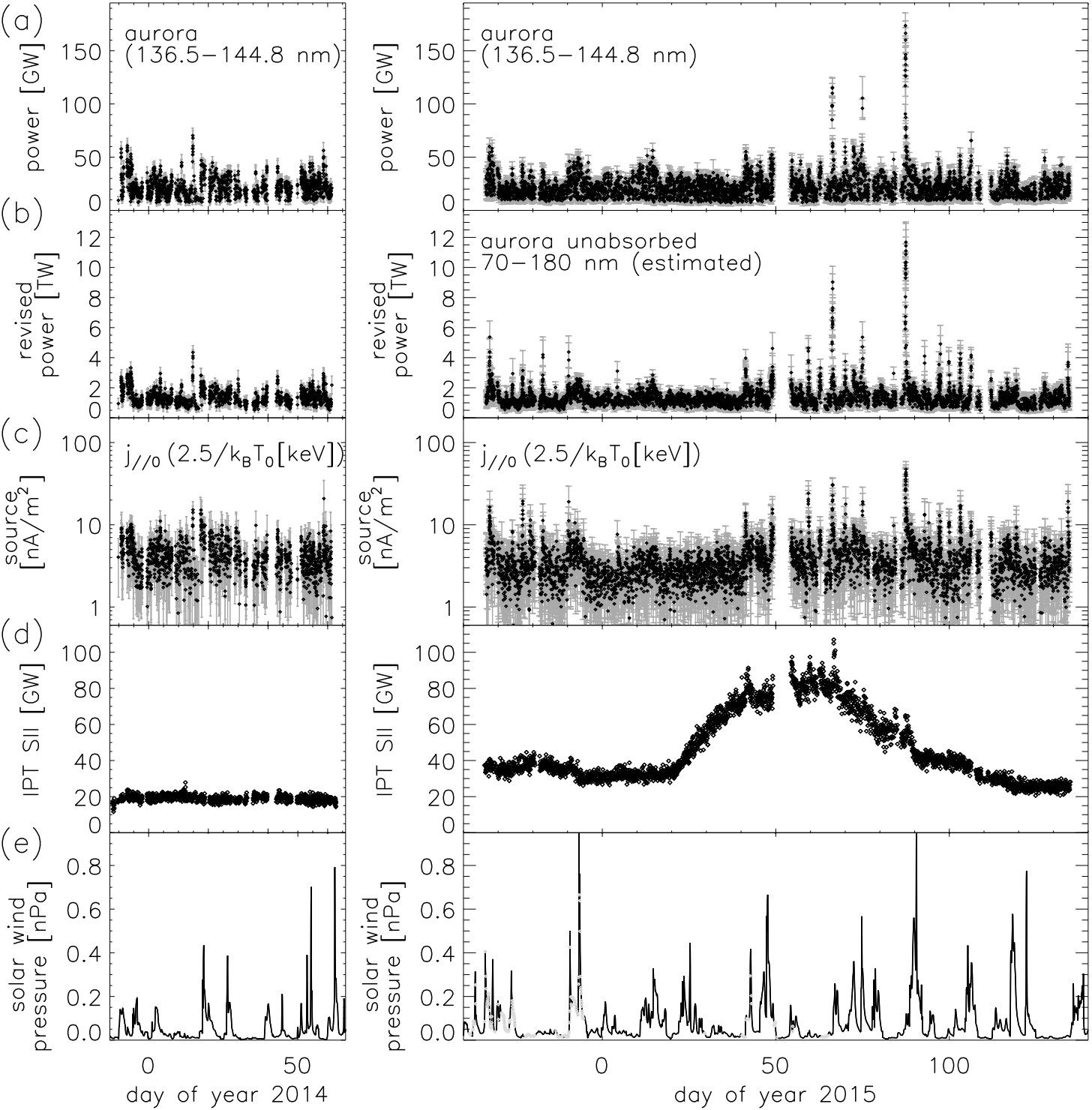
(a)
aurora
(136.5−144.8 nm)
power [GW]
150
100
50
0
(b)
revised
power [TW]
12
10
8
6
4
2
0
aurora unabsorbed
70−180 nm (estimated)
(c)
j//0 (2.5/k_B T_0[keV])
source
[nA/m^2]
100
10
1
(d)
IPT SII [GW]
100
80
60
40
20
0
(e)
solar wind
pressure [nPa]
0.8
0.6
0.4
0.2
0.0
0
50
100
day of year 2014
day of year 2015

Figure 2.

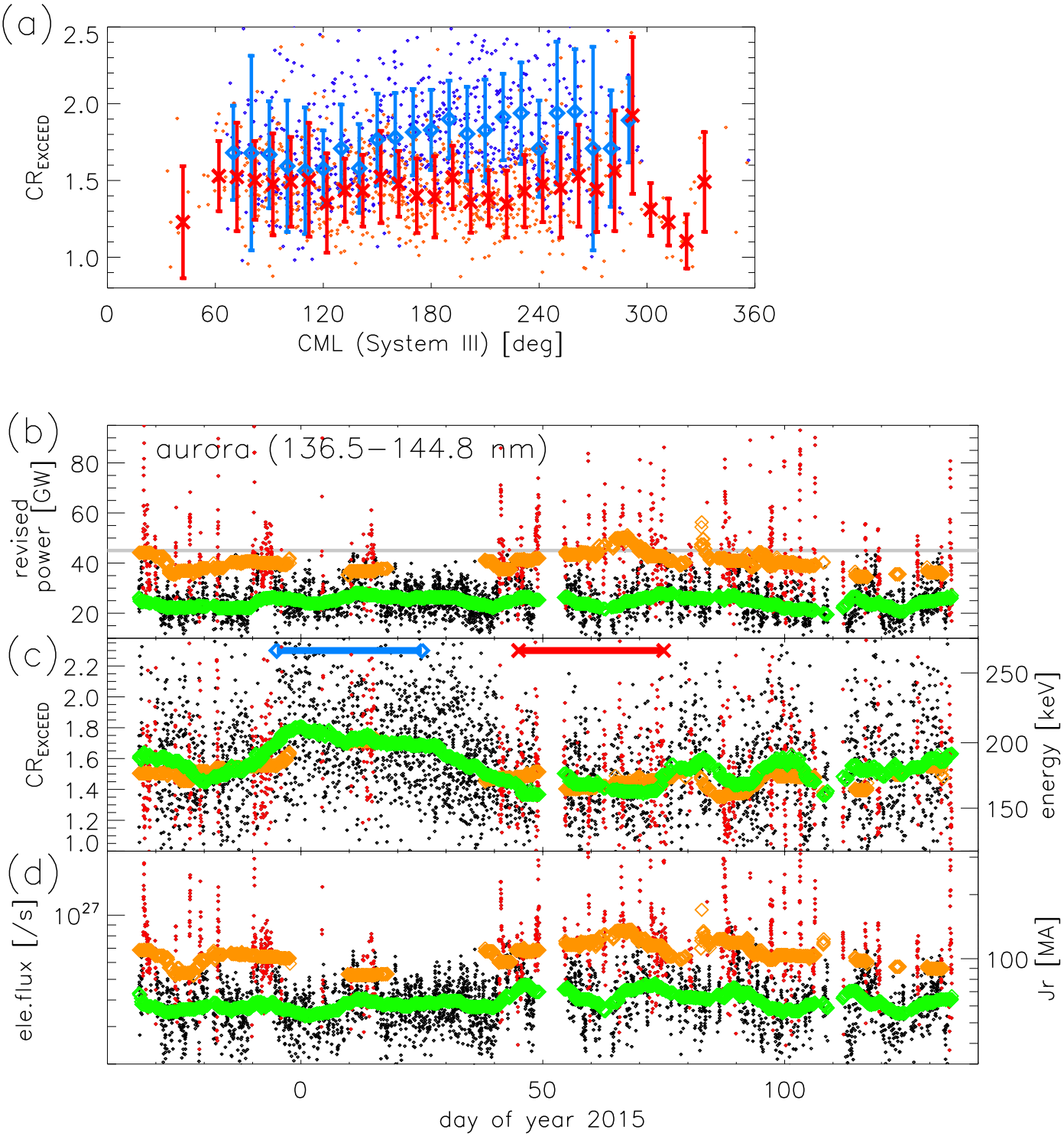
(a)
CR_EXCEED
2.5
2.0
1.5
1.0
0
60
120
180
240
300
360
CML (System III) [deg]
(b)
aurora (136.5−144.8 nm)
revised power [GW]
80
60
40
20
(c)
CR_EXCEED
2.2
2.0
1.8
1.6
1.4
1.2
1.0
250
200
150
energy [keV]
(d)
ele.flux [/s]
10^27
100
Jr [MA]
0
50
100
day of year 2015

Figure 3abc.

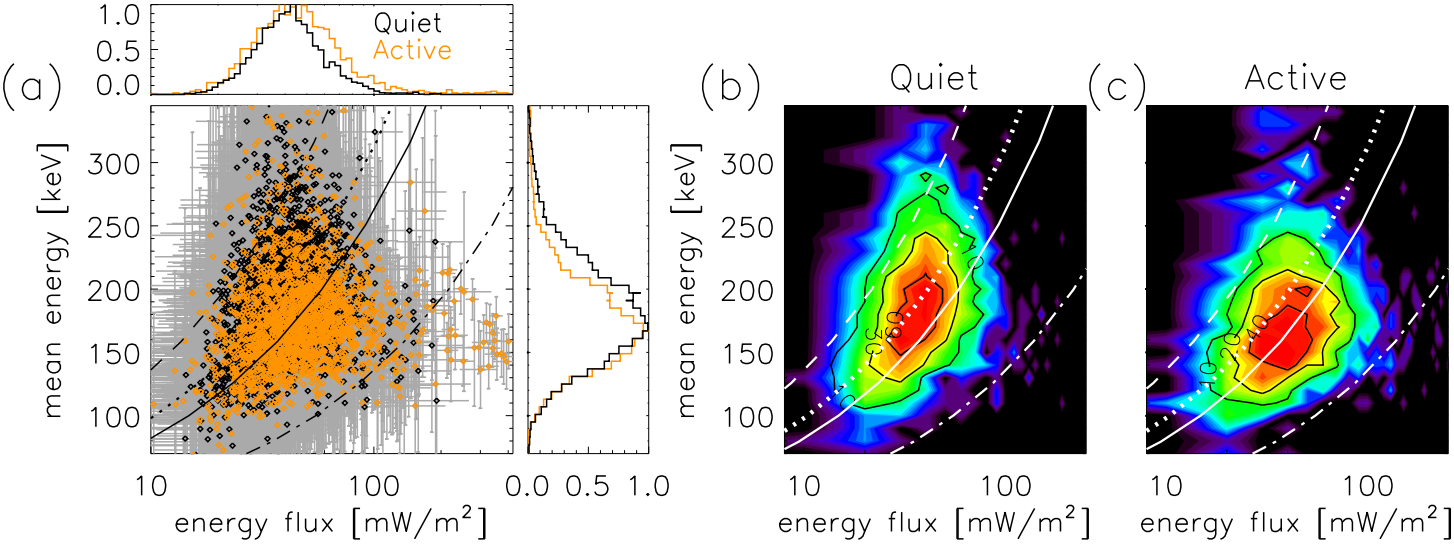
(a)
Quiet
Active
1.0
0.5
0.0
mean energy [keV]
300
250
200
150
100
10
100
0.0 0.5 1.0
energy flux [mW/m^2]
(b)
Quiet
mean energy [keV]
energy flux [mW/m^2]
(c)
Active
mean energy [keV]
energy flux [mW/m^2]

Figure 3de.

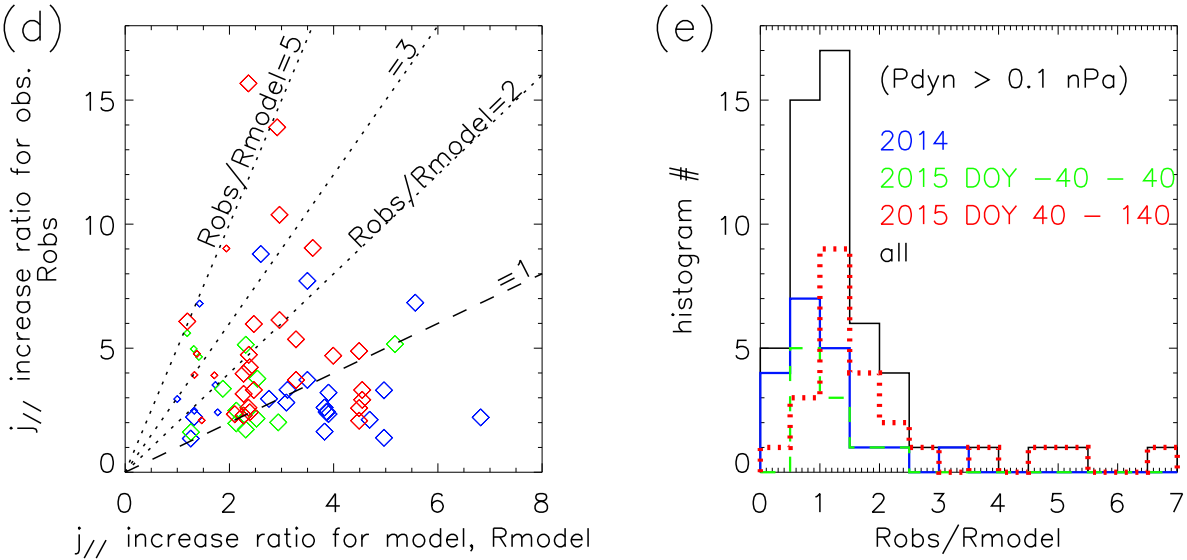
(d)
Robs/Rmodel=5
=3
Robs/Rmodel=2
=1
j// increase ratio for obs. Robs
j// increase ratio for model, Rmodel
0
2
4
6
8
0
5
10
15
(e)
(Pdyn > 0.1 nPa)
2014
2015 DOY −40 − 40
2015 DOY 40 − 140
all
histogram #
Robs/Rmodel
0
1
2
3
4
5
6
7
0
5
10
15